RESEARCH LETTER

Key Points:

- We develop and test a theory for the quantitative comparison of distributed and integrated fiber-optic strain sensing
- The sensitivity of integrated measurements depends primarily on local fiber curvature and fiber heterogeneity
- A data-based comparison corroborates the theory, thereby demonstrating the geophysical value of our integrated sensor system

Linking Distributed and Integrated Fiber-Optic Sensing

Daniel C. Bowden[1] [ID], **Andreas Fichtner[1]** [ID], **Thomas Nikas[2]** [ID], **Adonis Bogris[3]**, **Christos Simos[4]** [ID], **Krystyna Smolinski[1]** [ID], **Maria Koroni[1]** [ID], **Konstantinos Lentas[5]** [ID], **Iraklis Simos[6]** [ID], and **Nikolaos S. Melis[5]** [ID]

[1]Institute of Geophysics, ETH Zürich, Zürich, Switzerland, [2]Department of Informatics and Telecommunications, National and Kapodistrian University of Athens, Athens, Greece, [3]Department of Informatics and Computer Engineering, University of West Attica, Egaleo, Greece, [4]Electronics and Photonics Laboratory, Department of Physics, University of Thessaly, Lamia, Greece, [5]National Observatory of Athens, Institute of Geodynamics, Lofos Nimfon, Thission, Athens, Greece, [6]Department of Electrical and Electronics Engineering, University of West Attica, Egaleo, Greece

Abstract Distributed Acoustic Sensing (DAS) has become a popular method of observing seismic wavefields: backscattered pulses of light reveal strains or strain rates at any location along a fiber-optic cable. In contrast, a few newer systems transmit light through a cable and collect integrated phase delays over the entire cable, such as the Microwave Frequency Fiber Interferometer (MFFI). These integrated systems can be deployed over significantly longer distances, may be used in conjunction with live telecommunications, and can be significantly cheaper. However, they provide only a single time series representing strain over the entire length of the fiber. This work discusses theoretically how a distributed and integrated system can be quantitatively compared, and we note that the sensitivity depends strongly on points of curvature. Importantly, this work presents the first results of a quantitative, head-to-head comparison of a DAS and the integrated MFFI system using pre-existing telecommunications fibers in Athens, Greece.

Plain Language Summary New technologies are being developed to measure earthquakes using fiber-optic telecommunications cables. The most popular new method in recent years is "Distributed Acoustic Sensing," (DAS) in which pulses of light are repeatedly sent down a fiber and one measures the signals that reflect back. Shaking from an earthquake will stretch the fiber and the signature of reflected pulses will change. A new method (Microwave Frequency Fiber Interferometer [MFFI] in the paper) sends light from one end to the other and measures differences in optical phase. The new method has many advantages: it is cheaper, can be used on longer cables, and can be used at the same time as active telecommunications. As a disadvantage is lacks the high spatial resolution that DAS offers. This paper discusses the differences between the two methods and shows how to compare them, and then shows the first real-data, head-to-head comparison from an earthquake observed in Athens, Greece.

1. Introduction

Distributed Acoustic Sensing (DAS) has grown in application in recent years, as a method of measuring strains of a seismic wavefield. By sending pulses of light through a fiber-optic cable and measuring the changing signature of backscattered light, a single DAS interrogator can effectively measure strains or strain rates at thousands of locations along the fiber. Dense channel spacing on a meter scale and high sampling frequencies have made it attractive for seismological studies, including earthquake and aftershock monitoring (Li et al., 2021; Nayak et al., 2021), fault-zone imaging (Jousset et al., 2018; Lindsey et al., 2019), in boreholes (Lellouch et al., 2019), on glaciers (Walter et al., 2020), on volcanoes (Currenti et al., 2021; Fichtner, Klaasen, et al., 2022; Klaasen et al., 2021), and numerous others. Many such studies have exploited pre-existing telecommunications infrastructure, or "dark fibers" not in use; this potential has further enabled DAS observations in dense urban areas where characterizing seismic hazard is particularly important (Biondi et al., 2017; Martin et al., 2018; Yuan et al., 2020). It is precisely these urban areas where deploying new seismic instrumentation is challenging, and yet dense site-effect studies and microseismic monitoring are crucial.

Typical DAS systems are limited in the distance of fiber useable, however, listed by manufacturers usually in the tens of kilometers. There are limitations on how far the light can propagate before the backscattered signal is too attenuated and weak. Also a limiting factor is how long it takes for light to propagate back—a longer two-way

traveltime will mean the system has to wait longer before sending the next pulse, limiting the maximum sampling frequency.

In contrast, various systems have been proposed based on the transmission of light through a fiber, measuring the signal at the end (or after being looped back to the start). Such systems might exploit considerably longer fibers, offering seismologists a way to use existing transoceanic cables. Some authors have successfully measured polarization changes accumulated along the entire fibers (Mecozzi et al., 2021; Zhan et al., 2021), while others might measure changes in phase (Marra et al., 2018, 2022). Recently, Bogris et al. (2021) installed one such system in a suburban region of Athens, using pre-existing telecommunications fiber. Their particular system relies on the interferometric use of microwave-range frequencies-signals sent along the fiber and back in a closed loop are compared to what was sent and phase differences are measured. As with DAS, repeated observations allow them to measure changing strains along the fiber in real-time. Referred to as a Microwave Frequency Fiber Interferometer (MFFI), the system is a fraction of the cost of a typical DAS interrogator and can be used in parallel with live telecommunications signals.

A notable difference between the MFFI system (and all such phase transmission systems) as compared to DAS: the resulting observation is a single measure of strain integrated along the entire fiber length. This makes the measurement potentially harder for seismologists to interpret and to quantitatively compare to known types of data and acquisition systems.

In the first part of this paper, we give a conceptual description of the MFFI system and describe a theory based on standard continuum mechanics that allows us to relate DAS to the measurements of phase transmission systems.

In the second part, we report on a direct comparison experiment of DAS and MFFI. In September and October of 2021, we ran a Silixa iDAS interrogator alongside the MFFI system of Bogris et al. (2021) in northern Athens, Greece, in collaboration with the Hellenic Telecommunications Organization (in Greek: OTE). A number of earthquakes were observed, including both local and regional-scale events. We propose a way to integrate the many thousands of densely spaced DAS strain rate channels and thus recover what the MFFI system would observe, and subsequently find that the two systems agree remarkably well. This first quantitative comparison of integrated and distributed fiber-optic sensing validates the systems outputs, and solidifies our understanding of how physical wavefields in the Earth will be measured by emerging integrated sensing systems.

2. Relating Distributed and Integrated Deformation Sensors

In the following paragraphs, we provide a non-technical description of the MFFI system and some theoretical background of how its measurement of phase changes relates to fiber deformation, induced, for instance, by ground motion. This will then allow us to derive a relation between DAS and phase change measurements that permits a direct quantitative comparison.

2.1. Conceptual Introduction to MFFI

As described in the Introduction, the MFFI system of Bogris et al. (2021) measures phase changes collected along the entire route of fiber. A consistent, microwave-frequency sinusoidal signal is sent both along the fiber and directly to the measurement system, as in Figure 1. The signal returned from the fiber route is interferometrically compared to the starting signal, measuring the difference as a change in phase. This change in phase can be related to accumulated strain along the fiber. How that accumulated strain relates to the earth signal of interest and to the fiber geometry is the focus of the following section.

In principle, this type of measurement is consistent with systems employed by other authors, such as Marra et al. (2018, 2022), though the technical details of the systems will vary. Other authors measure accumulated changes in polarization as a different observable (Mecozzi et al., 2021; Zhan et al., 2021), but even then, the resulting measurement of interest to geoscientists remains one of integrated strain or strain rate.

2.2. Exact Relations Between Fiber Deformation and Optical Phase Changes

Before trying to find a quantitative relation between DAS and phase transmission systems such as MFFI, we consider the dependence of the optical phase $\phi(t)$ on the deformation tensor $\boldsymbol{F}(\boldsymbol{x}, t)$ along the fiber. A more
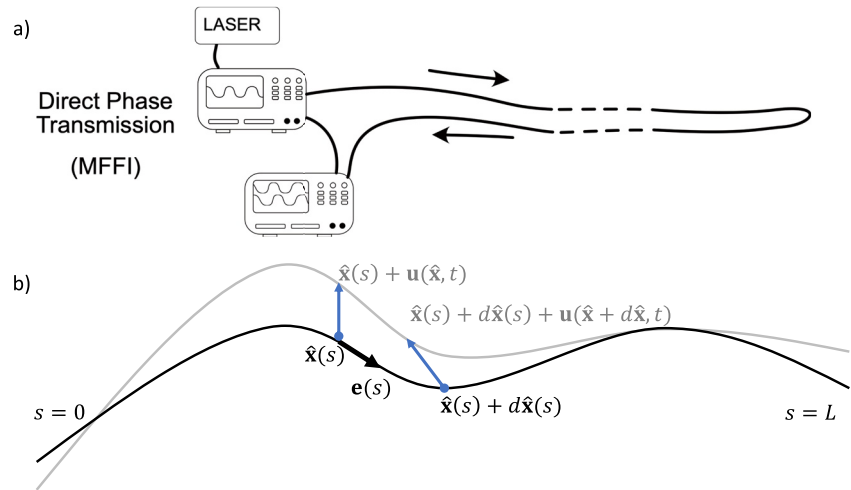
Figure 1. (a) A simplified schematic of the Microwave Frequency Fiber Interferometer (MFFI) system to accompany Section 2.1. A microwave frequency signal is sent along the fiber and returned to the lab, where phase differences are measured. (b) Schematic illustration of fiber deformation for Section 2.2. The undeformed fiber, shown as black curve, is represented by the position vector $\hat{\mathbf{x}}(s)$, which is parametrized in terms of the arc length s. The cable starts at $s = 0$ and ends at $s = L$. Under a displacement field $\mathbf{u}(\hat{\mathbf{x}}, t)$, displayed as blue arrows, the Lagrangian position $\hat{\mathbf{x}}(s)$ along the undeformed fiber moves to $\hat{\mathbf{x}}(s) + d\hat{\mathbf{x}}(s)$. The result is the deformed fiber, shown in gray. The local tangent vector $\mathbf{e}(s)$ is shown as a thick black arrow. Panel (b): Fiber deformation leads to both a change in length and refractive index (light speed). The latter is referred to as the photo-elastic effect.

detailed version of the following paragraphs can be found in Fichtner, Bogris, Nikas, et al. (2022). The only assumption is that the traveltime of the pulse is much smaller than the characteristic time scales of deformation, meaning that the fiber does not deform significantly while a pulse is propagating. We adopt a parameterized representation of the fiber, with its position $\hat{\mathbf{x}}(s)$ given in terms of the arc length s. The latter ranges between 0 and the total length of the fiber L, as shown in Figure 1.

In the undeformed state, the time it takes for a pulse to travel from fiber location $\hat{\mathbf{x}}(s)$ to the neighboring location $\hat{\mathbf{x}}(s) + d\hat{\mathbf{x}}(s)$ is given by $dT = |d\hat{\mathbf{x}}(s)|/c[\hat{\mathbf{x}}(s)]$, where $c[\hat{\mathbf{x}}(s)]$ is the potentially space-dependent speed of light along the fiber. By definition of the arc length, we can express the total traveltime of the pulse as $T = \int_{s=0}^{L} c^{-1}[\hat{\mathbf{x}}(s)]\, ds$. Under deformation, position $\hat{\mathbf{x}}$ moves to $\hat{\mathbf{x}} + \mathbf{u}(\hat{\mathbf{x}}, t)$, where $\mathbf{u}(\hat{\mathbf{x}}, t)$ is the (seismic) displacement field, as illustrated in Figure 1. The neighboring point at the original position $\hat{\mathbf{x}} + d\hat{\mathbf{x}}$ moves to $\hat{\mathbf{x}} + d\hat{\mathbf{x}} + \mathbf{u}(\hat{\mathbf{x}} + d\hat{\mathbf{x}}, t)$. It follows that the traveltime of the pulse within the deformed segment of the cable is now

$$dT(t) = \frac{|d\hat{\mathbf{x}} + \mathbf{u}(\hat{\mathbf{x}} + d\hat{\mathbf{x}}, t) - \mathbf{u}(\hat{\mathbf{x}}, t)|}{c[\hat{\mathbf{x}}, \mathbf{u}(\hat{\mathbf{x}}, t)]}. \tag{1}$$

The denominator accounts for the photo-elastic effect, i.e., changes in the speed of light induced by deformation. Since $d\hat{\mathbf{x}}$ is infinitesimally small, we can rewrite the numerator as:

$$\mathbf{u}(\hat{\mathbf{x}} + d\hat{\mathbf{x}}, t) - \mathbf{u}(\hat{\mathbf{x}}, t) = \mathbf{F}(\hat{\mathbf{x}}, t)\, d\hat{\mathbf{x}}, \tag{2}$$

where the components of the deformation tensor $\mathbf{F}$ are defined by $F_{ij} = \partial u_i/\partial x_j$. In terms of $\mathbf{F}$, we can rewrite (Equation 1) as

$$dT(t) = \frac{|d\hat{\mathbf{x}} + \mathbf{F}(\hat{\mathbf{x}}, t)\, d\hat{\mathbf{x}}|}{c[\hat{\mathbf{x}}, \mathbf{u}(\hat{\mathbf{x}}, t)]}. \tag{3}$$

This can be further simplified using the arc-length parametrization of the position vector, $d\hat{\mathbf{x}} = \mathbf{e}(s)\, ds$, where $\mathbf{e}(s)$ is the normalized tangent vector along the fiber. With this, we find

$$dT(t) = \frac{\left| \left[\mathbf{I} + \mathbf{F}\left(\hat{\mathbf{x}}, t\right) \right] \mathbf{e}(s) \right|}{c \left[\hat{\mathbf{x}}, \mathbf{u}\left(\hat{\mathbf{x}}, t\right) \right]} \, ds, \tag{4}$$

and the total, time-dependent traveltime of the pulse becomes

$$T(t) = \int_{s=0}^{L} \frac{\left| \left[\mathbf{I} + \mathbf{F}\left(\hat{\mathbf{x}}, t\right) \right] \mathbf{e}(s) \right|}{c \left[\hat{\mathbf{x}}, \mathbf{u}\left(\hat{\mathbf{x}}, t\right) \right]} \, ds. \tag{5}$$

In the specific case of a monochromatic input with circular frequency ω, the traveltime difference $\Delta T(t) = T(t) - T$ translates into a phase difference $\phi(t) = \omega \Delta T(t)$ between the reference and the deformed state. Taking the time derivative to measure phase changes (which the MFFI system actually measures), the constant T drops away and we obtain:

$$\partial_t \phi(t) = \omega \partial_t \int_{s=0}^{L} \frac{\left| \left[\mathbf{I} + \mathbf{F}\left(\hat{\mathbf{x}}, t\right) \right] \mathbf{e}(s) \right|}{c \left[\hat{\mathbf{x}}, \mathbf{u}\left(\hat{\mathbf{x}}, t\right) \right]} \, ds. \tag{6}$$

Equation 6 is valid without any approximations, and it relates measured phase changes of the monochromatic laser signal to the deformation field $\mathbf{u}\left(\hat{\mathbf{x}}, t\right)$ along the fiber.

2.3. First-Order Approximations and Relations to DAS

Equation 6 can be simplified considerably by realizing that typical seismic displacement fields $\mathbf{u}$ have amplitudes in the nano- or micrometer range. Therefore, the norm of the deformation tensor $\mathbf{F}$ is typically orders of magnitude smaller than 1. It follows that first-order approximations can easily be justified. To avoid clumsy notation, we work with a slight reformulation of Equation 6, which uses the refractive index $n = c_0/c$, where c_0 is the speed of light in vacuum. To simplify (Equation 6), we employ the first-order approximation

$$\left| \left[\mathbf{I} + \mathbf{F}\left(\hat{\mathbf{x}}, t\right) \right] \mathbf{e}(s) \right|^2 \approx 1 + 2\mathbf{e}^T \mathbf{E} \mathbf{e}, \tag{7}$$

with the strain tensor $\mathbf{E} = (\mathbf{F}^T + \mathbf{F})/2$. Denoting the strain along the fiber as $\epsilon = \mathbf{e}^T \mathbf{E} \mathbf{e}$ and using the first-order relation $\sqrt{1 + 2\epsilon} \doteq 1 + \epsilon$, we arrive at

$$\partial_t \phi(t) \approx \frac{\omega}{c_0} \partial_t \int_{s=0}^{L} n \left[\hat{\mathbf{x}}, \mathbf{u}\left(\hat{\mathbf{x}}\right) \right] \left(1 + \epsilon \left[\hat{\mathbf{x}}(s), t \right] \right) \, ds. \tag{8}$$

Assuming that n primarily depends on ϵ, we may use the first-order Taylor expansion $n(\epsilon) \doteq n_0 + n'\epsilon$, thereby obtaining

$$\partial_t \phi(t) \approx \frac{\omega}{c_0} \partial_t \int_{s=0}^{L} \tilde{n}\left[\hat{\mathbf{x}}(s) \right] \epsilon \left[\hat{\mathbf{x}}(s), t \right] \, ds, \tag{9}$$

where $\tilde{n} = n_0 + n'$ is the sum of the static refractive index and the axial strain derivative of the refractive index. The latter is referred to as the photoelastic effect of the material, and has been experimentally shown to contribute around 20% of the amplitude compared to length changes of the fiber (Bertholds & Dändliker, 1988). Regardless of how that refractive index is measured, Equation 9 provides a direct relation between phase changes $\partial_t \phi$ measured by the transmission system, and the axial strain rate $\partial_t \epsilon$. In the case where the refractive index is roughly constant along the fiber, it suffices to integrate DAS measurements of $\partial_t \epsilon$ along the fiber in order to synthesize transmission measurements of $\partial_t \phi$. In practice, integrating is achieved by simply summing all the individual DAS channels. While the integration in Equation 9 may seem intuitively clear, its simplicity is nevertheless pleasantly surprising, given that it incorporates effects related to changes in both fiber length and refractive index.

In the hypothetical case that an entire fiber was perfectly straight, Equation 9 reduces to a measure of strain between the start and ending points; an integral over a derivative reduces to zero everywhere else. In a sense, that hypothetical situation may be considered analogous to the gauge-length effects known to the DAS community (Lindsey & Martin, 2021) where a given segment of DAS is assumed to be straight. However, as shown in more detail in Fichtner, Bogris, Nikas, et al. (2022), points of fiber curvature are crucial for observing strains since it
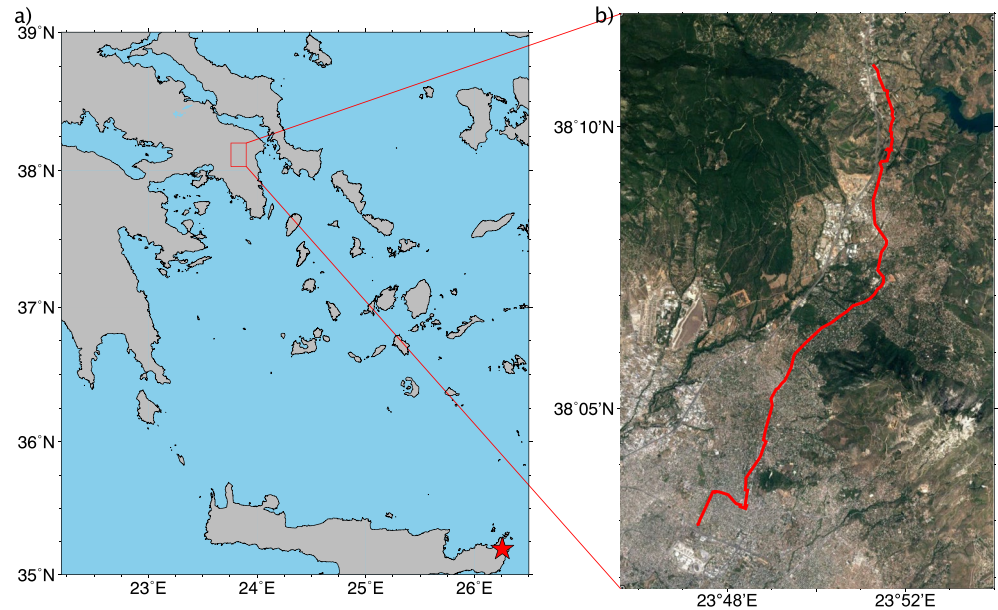
Figure 2. The location of the fiber-optic cables used in Greece. Panel (a) shows a broad part of Greece and the Aegean Sea, with a red star indicating the epicenter of the *M* 6.3 earthquake discussed later and a red box indicating the region expanded in the next panel. Panel (b) shows a region of northern Athens and the cable containing both the distributed acoustic sensing (DAS) and Microwave Frequency Fiber Interferometer (MFFI).

is only at such locations where the fibers see differing contributions from the wavefield. This means that interpreting the signal from such a system is both complex and offers opportunity for new analysis since the variable sensitivities along a fiber can be exploited (Fichtner, Bogris, Bowden, et al., 2022).

3. Experimental Comparison of Integrated and Distributed Sensing

From the theory above (specifically Equation 9), we see that we can directly compare a DAS system to the MFFI output. In September and October of 2021, we operated a Silixa iDAS interrogator alongside the system described by Bogris et al. (2021). Both systems used pre-existing telecommunications fiber in collaboration with the Hellenic Telecommunications Organization (OTE), and the work was completed with assistance from the National Observatory of Athens. Figure 2 shows the extent of the fiber, with both the DAS interrogator and the transmission interferometer housed at the OTE Academy building at the southwest end. The total length of fiber used for the DAS measurements was roughly 24 km, while the transmission-based system followed the same path and then was looped back to return to the starting location. This extra travel path is accounted for when converting optical phase delays to strain rate (Bogris et al., 2021).

Several earthquakes occurred during the time in which both systems were running. Notably, an earthquake of ML 6.3 occurred on October 12th near the island of Crete, roughly 380 km to the southeast (red star in Figure 2). Despite the distance, the earthquake resulted in ground motions in Athens as strong as 0.1 cm/s as reported on a nearby strong motion sensor, HL.PLT, operated by the National Observatory of Greece (National Observatory of Athens, Institute of Geodynamics, Athens, 1975).

Figure 3 shows the individual DAS channels along the fiber, while Figure 4 shows the comparison between systems. Individual DAS channels in Figure 3 are integrated (summed) to produce the orange time series in Figure 4, while the blue time series represents the output from the MFFI system of Bogris et al. (2021). We see that the strain rates measured by the two systems agree to within the pre-event noise at both lower frequencies (Panel a) and higher frequencies (Panel b). This includes strong agreement of the timing of seismic phases between the two systems.

The overall amplitude of the averaged DAS signals and the MFFI output are rather smaller than any individual DAS channel. We expect that averaging the many local strains will lead to constructive and destructive
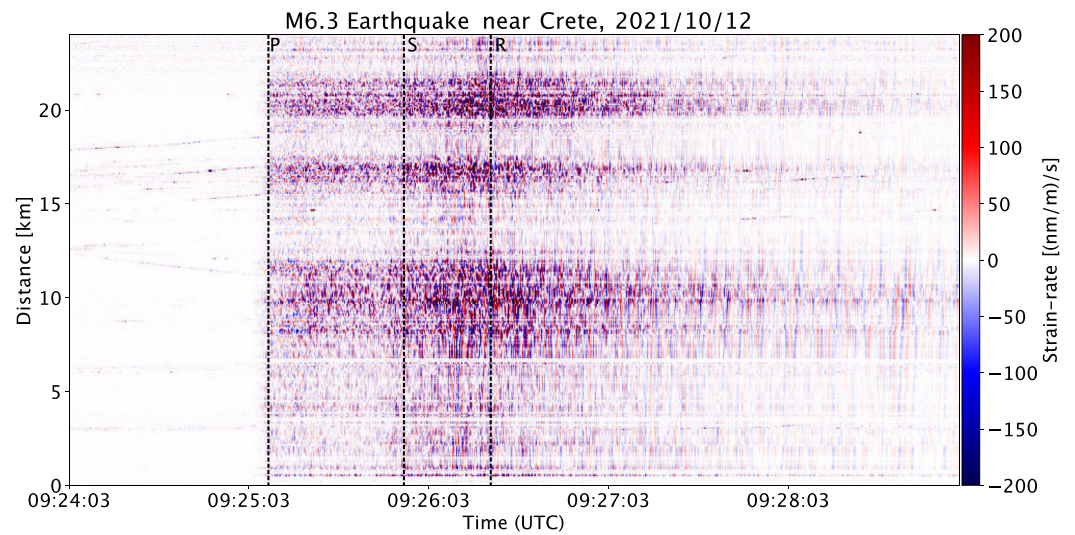
Figure 3. The ML 6.3 Crete earthquake as recorded by the distributed acoustic sensing (DAS) system, recorded with a 2 m channel spacing. The data is broadly filtered between 0.05 and 5 Hz. Vertical dashed lines indicate the estimated *P*-, *S*-, and Rayleigh-wave arrival times.
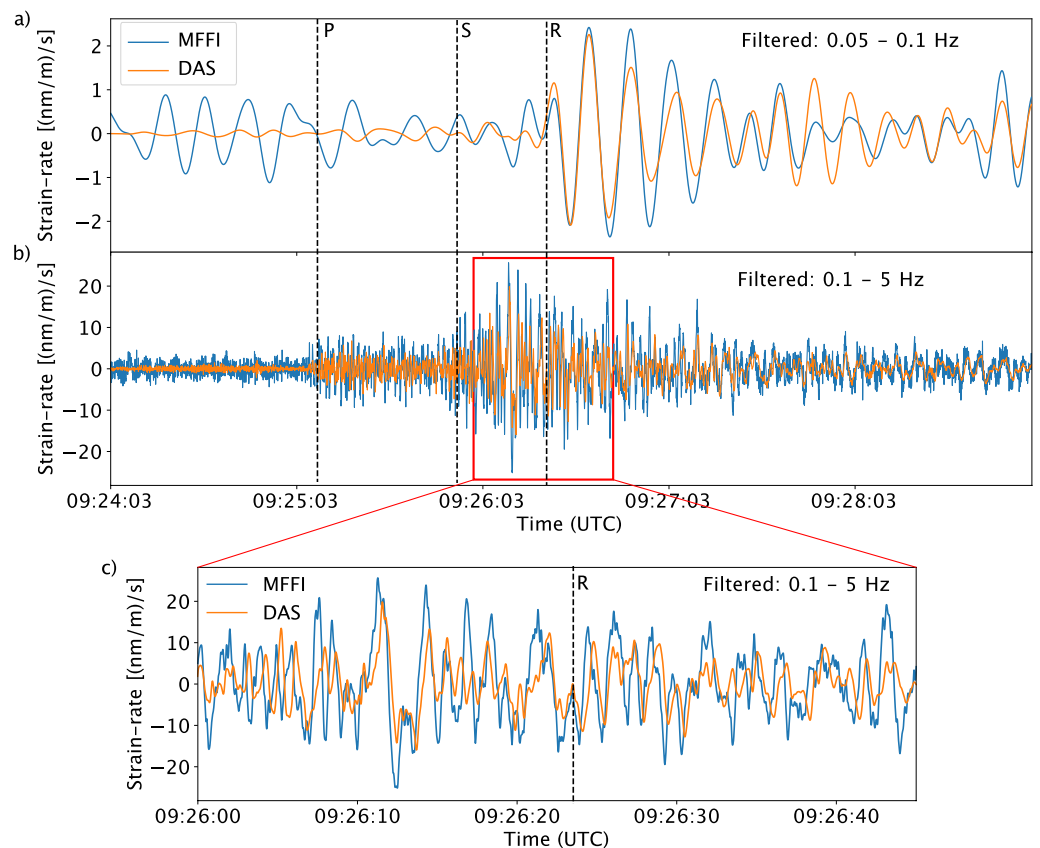

Figure 4. The ML 6.3 Crete earthquake as recorded by both systems. distributed acoustic sensing (DAS) channels are integrated to produce the orange time series, and the Microwave Frequency Fiber Interferometer (MFFI) outputs are in blue. Panel (a) shows signals at a lower frequency range of 0.05–0.1 Hz, while Panels (b and c) show a higher frequency range of 0.1–5 Hz. Panel (c) zooms in on a narrower time range of the signals in Panel (b). Vertical dashed lines indicate the estimated *P*-, *S*-, and Rayleigh-wave arrival times.
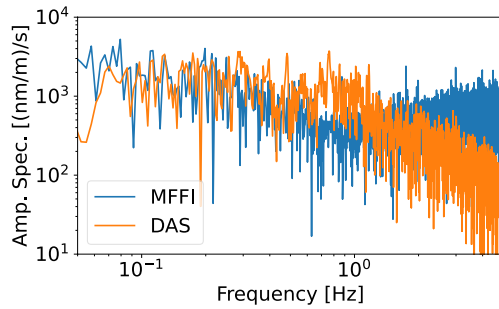
Figure 5. The ML 6.3 Crete earthquake as recorded by both systems, here in the frequency domain.

interference, since the various phases arrive at different sections of the cable at different times, resulting in a total signal that is lower in amplitude. Fortunately, non-coherent signals such as those resulting from local urban noise and cars are also expected to be relatively suppressed compared to an individual DAS trace.

Also, as with many DAS studies, in Figure 3 we observe regions where DAS strain rates are stronger or weaker. This may be a result of any number of factors, for example, from local soil conditions and site amplifications, local coupling of the fiber to the ground, or varying directions of the fiber relative to the incident phases. This does not pose an issue for our comparison of the two systems since the MFFI system uses the same cable, but we note that these sensitivities will be important to characterize if earthquake magnitudes are to be related to strains in the future (Lior et al., 2021).

Regarding the seismic energy observed in Figure 4, it is not precise to interpret in the sense of distinct seismic arrivals as seismologists may be accustomed to. Generally, we believe the longer period signals (panel a) are dominated by surface waves, while the higher frequency signals (panels b, c) are dominated by *P*- and *S*-waves. The dashed lines indicate estimated arrival times using TauP (Crotwell et al., 1999) with AK135 as a reference model for the *P*- and *S*-waves (Kennett et al., 1995), and a constant Rayleigh-wave velocity of 2.75 km/s, roughly appropriate for a 10 s period. In fact, the surface wave contribution should also include Love-wave energy, given the varied orientation of the cable, but we do not focus on separating or distinguishing the two in this paper. These arrivals also agree with the interpretation of stronger *P* and *S* waves observed in the DAS traces from Figure 3. However, given the fact that the MFFI signal represents an integral of strains across the entire fiber loop, it likely includes multiple distinct seismic arrivals reaching different sections of the fiber at different times, potentially overlapping with one another. It is precisely this difference in timing which is exploited in the interferometric approach outlined by (Fichtner, Bogris, Bowden, et al., 2022).

When considering the spectra of both systems, we again see a remarkable similarity in reported strain rates as in Figure 5. The signals agree very well in the range of 0.1–0.6 Hz, above which the DAS system retains slightly higher amplitudes until roughly 1 Hz. We expect that the DAS is still recovering realistic signals still above 1 Hz, but that the earthquake source corner frequency and attenuation mean the signals are weaker at higher frequencies (Lior et al., 2021). The MFFI system shows a linear increase at higher frequencies, but this is expected to be system noise given the limitations of the devices used in that prototype (Bogris et al., 2021). Notably, their system used an inexpensive Arduino Analog-to-Digital Converter during this development phase, but such limitations can be overcome in future iterations.

4. Discussion and Conclusions

We developed exact and first-order theories for integrated fiber-optic deformation sensing. The resulting equations enable a quantitative comparison with distributed strain sensing (DAS), and we emphasize the dependence of the integrated measurements on fiber curvature and heterogeneity.

Parallel experiments for integrated and distributed sensing performed in Athens, using pre-existing telecommunication fibers, allow us to verify the theory with real data and to compare the two systems. The systems report quantitatively similar measurements of strain rates from a moderately sized, regional earthquake, in both time and frequency domain. Although earlier studies have demonstrated the feasibility of integrated fiber sensing systems (Marra et al., 2018; Mecozzi et al., 2021; Zhan et al., 2021), this comparison to DAS provides a crucial step for seismologists to understand and quantitatively interpret such observations in the future.

The fact that the integrated system's sensitivity is highly dependent on curvature means one could miss small ground-motion events. In the case of small events along a straight fiber section, we expect that little to no total strain measurement would appear. Only in cases where such small waves reached a place where the cable bends, or else one of the terminus points, would an integrated strain signal be present. This means care needs to be taken

when choosing pre-existing fibers or when designing new systems, or alternatively one needs to at least be aware of the potential spatial gaps in one's coverage.

We envision that future seismological studies will exploit a range of complementary sensor types at different scales: DAS or dense geophone arrays for very spatially dense wavefield observations (Muir & Zhan, 2021); existing broadband seismic networks for high-precision, but spatially sparse observations, or similarly point-measurement interferometers at the terminal end of a fiber-optic cable (Seat et al., 2015); and finally, integrated strain sensing systems like MFFI for observations over particularly long distances, or particularly hard-to-reach locations (e.g., offshore). Recent work by Marra et al. (2022) also indicates the feasibility of using a direct-transmission phase system, interspersed with telecommunication repeaters to recover further spatial localization of signals. Finally, we note that it has already been shown that mixed-instrument arrays can be used for even relatively complex, full-waveform analysis (Paitz et al., 2019), and also that integrated strain sensing systems like MFFI can fit into this same framework for interferometry (Fichtner, Bogris, Bowden, et al., 2022).

Integrated strain sensing systems, such as the MFFI system designed by Bogris et al. (2021), are especially exciting in the context of pre-existing telecommunications fibers already connecting our cities. The fact that it can be deployed cheaply and using live telecommunications networks means multiple systems could quickly blanket large regions of the Earth's surface. Such prospects have been often proposed by the DAS community, and we expect that will remain desirable for high-resolution application, but the flexibility and cost-effectiveness of MFFI makes it an attractive counterpart. The fact that it can now be quantitatively interpreted and understood paves the way for these kinds of systems being incorporated into existing seismological frameworks for earthquake detection and location, tomography, and natural hazard monitoring.

Data Availability Statement

Data from both systems is available from the ETH research collection at https://doi.org/10.3929/ethz-b-000558252, along with Python Jupyter notebooks to reproduce the figures. Maps were made with PyGMT (Uieda et al., 2021), and satellite imagery is from Google Earth. Seismic arrival times are estimated with the TauP implementation in ObsPy, from https://docs.obspy.org/.

References

Bertholds, A., & Dändliker, R. (1988). Determination of the individual strain-optic coefficients in single-mode optical fibers. *Journal of Lightwave Technology*, *6*(1), 17–20. https://doi.org/10.1109/50.3956

Biondi, B., Martin, E., Cole, S., Karrenbach, M., & Lindsey, N. (2017). Earthquakes analysis using data recorded by the Stanford DAS Array. SEG Technical Program Expanded Abstracts (September 2016), (pp. 2752–2756). https://doi.org/10.1190/segam2017-17745041.1

Bogris, A., Simos, C., Simos, I., Nikas, T., Melis, N. S., Mesaritakis, C., et al. (2021). Microwave frequency dissemination systems as sensitive and low-cost interferometers for earthquake detection on commercially deployed fiber cables. *arXiv*, (1), 10–12. https://doi.org/10.48550/arXiv.2111.02957

Crotwell, H. P., Owens, T. J., & Ritsema, J. (1999). The TauP toolkit: Flexible seismic traveltime and raypath utilities. *Seismological Research Letters*, *70*, 154–160. https://doi.org/10.1785/gssrl.70.2.154

Currenti, G., Jousset, P., Napoli, R., Krawczyk, C., & Weber, M. (2021). On the comparison of strain measurements from fiber-optics with a dense seismometer array at Etna volcano (Italy). *Solid Earth*, *12*(4), 993–1003. https://doi.org/10.5194/se-12-993-2021

Fichtner, A., Bogris, A., Bowden, D. C., Lentas, K., Melis, N. S., Simos, C., et al. (2022). Sensitivity kernels for transmission fiber-optics. in Review, arXiv. https://doi.org/10.48550/arXiv.2203.05229

Fichtner, A., Bogris, A., Nikas, T., Bowden, D., Lentas, K., Melis, N. S., et al. (2022). Theory of phase transmission fiber-optic deformation sensing. *Geophysical Journal International*, *231*(2), 1031–1039. https://doi.org/10.1093/gji/ggac237

Fichtner, A., Klaasen, S., Thrastarson, S., Cubuk-Sabuncu, Y., Paitz, P., & Jonsdottir, K. (2022). Fiber-optic observation of volcanic tremor through floating ice-sheet resonance. *The Seismic Record*, *2*(3), 148–155. https://doi.org/10.1785/0320220010

Jousset, P., Reinsch, T., Ryberg, T., Blanck, H., Clarke, A., Aghayev, R., et al. (2018). Dynamic strain determination using fiber-optic cables allows imaging of seismological and structural features. *Nature Communications*, *9*(1). https://doi.org/10.1038/s41467-018-04860-y

Kennett, B. L. N., Engdahl, E. R., & Buland, R. (1995). Constraints on seismic velocities in the Earth from traveltimes. *Geophysical Journal International*, *122*(1), 108–124. https://doi.org/10.1111/j.1365-246x.1995.tb03540.x

Klaasen, S., Paitz, P., Lindner, N., Dettmer, J., & Fichtner, A. (2021). Distributed acoustic sensing in volcano-glacial environments—Mount Meager, British Columbia. *Journal of Geophysical Research: Solid Earth*, *126*(11). https://doi.org/10.1029/2021JB022358

Lellouch, A., Yuan, S., Ellsworth, W. L., & Biondi, B. (2019). Velocity-based earthquake detection using downhole distributed acoustic sensing—Examples from the San Andreas fault observatory at depth. *Bulletin of the Seismological Society of America*, *109*(6), 2491–2500. https://doi.org/10.1785/0120190176

Li, Z., Shen, Z., Yang, Y., Williams, E., Wang, X., & Zhan, Z. (2021). Rapid response to the 2019 Ridgecrest earthquake with distributed acoustic sensing. *AGU Advances*, *2*(2), e2021AV000395. https://doi.org/10.1029/2021av000395

Lindsey, N. J., Dawe, T. C., & Ajo-franklin, J. B. (2019). Illuminating seafloor faults and ocean dynamics with dark fiber distributed acoustic sensing. *Science*, *1107*(6469), 1103–1107. https://doi.org/10.1126/science.aay5881

Lindsey, N. J., & Martin, E. R. (2021). Fiber-optic seismology (pp. 309–336).

Lior, I., Sladen, A., Mercerat, D., Ampuero, J.-p., Rivet, D., & Sambolian, S. (2021). Strain to ground motion conversion of distributed acoustic sensing data for earthquake magnitude and stress drop determination. *Solid Earth*, *12*(6), 1421–1442. https://doi.org/10.5194/se-12-1421-2021

Marra, G., Clivati, C., Luckett, R., Tampellini, A., Kronjäger, J., Wright, L., et al. (2018). Ultrastable laser interferometry for earthquake detection with terrestrial and submarine cables. *Science*, *490*, 486–490. https://doi.org/10.1126/science.aat4458

Marra, G., Fairweather, D. M., Kamalov, V., Gaynor, P., Cantono, M., Mulholland, S., et al. (2022). Optical interferometry-based array of seafloor environmental sensors using a transoceanic submarine cable. *Science*, *376*(6595), 874–879. https://doi.org/10.1126/science.abo1939

Martin, E. R., Huot, F., Ma, Y., Cieplicki, R., Cole, S., Karrenbach, M., & Biondi, B. L. (2018). A seismic shift in scalable acquisition demands new processing: Fiber-optic seismic signal retrieval in urban areas with unsupervized learning for coherent noise removal. *IEEE Signal Processing Magazine*, *35*(2), 31–40. https://doi.org/10.1109/msp.2017.2783381

Mecozzi, A., Cantono, M., Castellanos, J. C., Kamalov, V., Muller, R., & Zhan, Z. (2021). Polarization sensing using submarine optical cables. *Optica*, *8*(6), 6–13. https://doi.org/10.1364/optica.424307

Muir, J. B., & Zhan, Z. (2021). Wavefield-based evaluation of DAS instrument response and array design. *Geophysical Journal International*, *229*(1), 21–34. https://doi.org/10.1093/gji/ggab439

National Observatory of Athens, Institute of Geodynamics, Athens. (1975). *National Observatory of Athens Seismic Network*. International Federation of Digital Seismograph Networks. Retrieved from https://www.fdsn.org/networks/detail/HL/ https://doi.org/10.7914/SN/HL

Nayak, A., Ajo-franklin, J., & The Imperial Valley Dark Fiber Team. (2021). Distributed acoustic sensing using dark fiber for array detection of regional earthquakes. *Seismological Research Letters*, *92*(4), 2441–2452. https://doi.org/10.1785/0220200416

Paitz, P., Sager, K., & Fichtner, A. (2019). Rotation and strain ambient noise interferometry. *Geophysical Journal International*, *216*(3), 1938–1952. https://doi.org/10.1093/gji/ggy528

Seat, H. C., Cattoen, M., Lizion, F., Suleiman, M., Boudin, F., Brunet, C., et al. (2015). A fiber Fabry-Perot interferometer for geophysics applications. *IEEE Sensors*, 1–4. https://doi.org/10.1109/ICSENS.2015.7370316

Ueda, L., Tian, D., Leong, W. J., Jones, M., Schlitzer, W., Toney, L., et al. (2021). *PyGMT: A Python interface for the generic mapping tools*. Zenodo. https://doi.org/10.5281/zenodo.5607255

Walter, F., Gräff, D., Lindner, F., Paitz, P., Köpfli, M., Chmiel, M., & Fichtner, A. (2020). Distributed acoustic sensing of microseismic sources and wave propagation in glaciated terrain. *Nature Communications*, *11*(2436). https://doi.org/10.1038/s41467-020-15824-6

Yuan, S., Lellouch, A., Clapp, R. G., & Biondi, B. (2020). Near-surface characterization using a roadside distributed acoustic sensing array. *The Leading Edge*, *39*(9), 646–653. https://doi.org/10.1190/tle39090646.1

Zhan, Z., Cantono, M., Kamalov, V., Mecozzi, A., Müller, R., Yin, S., & Castellanos, J. C. (2021). Optical polarization-based seismic and water wave sensing on transoceanic cables. *Science*, *371*(6532), 931–936. https://doi.org/10.1126/science.abe6648